

Article

Refined Simulation of Reinforced Concrete Beam Based on a Hybrid Peridynamic Method

Chun Lin ¹, Zhe Lin ², Xin Xue ², Song He ^{3,4,5,6} and Lei Wang ^{3,4,5,7,*}¹ School of Architecture, Huaqiao University, Xiamen 361021, China; chunlin@hqu.edu.cn² School of Architecture and Civil Engineering, Xiamen University, Xiamen 361021, China; zhelin98@stu.xmu.edu.cn (Z.L.); xuexin@xmu.edu.cn (X.X.)³ College of Architecture and Civil Engineering, Wenzhou University, Wenzhou 325035, China; 20210465@wzu.edu.cn⁴ Key Laboratory of Engineering and Technology for Soft Soil Foundation and Tideland Reclamation of Zhejiang Province, Wenzhou 325035, China⁵ Wenzhou Engineering Technical Research Center on Building Energy Conservation and Emission Reduction & Disaster Prevention and Mitigation, Wenzhou 325035, China⁶ Zhejiang International Science and Technology Cooperation Base of Ultra-Soft Soil Engineering and Smart Monitoring, Wenzhou 325035, China⁷ Zhejiang Engineering Research Center of Disaster Prevention and Mitigation for Coastal Soft Soil Foundation, Wenzhou 325035, China

* Correspondence: leiwang@wzu.edu.cn

Abstract: Reinforced concrete (RC) structures under earthquake excitation may fail and cause significant casualties and economic losses, highlighting the importance of studying their seismic failure mechanisms. Considering that the commonly used finite element method and discrete element method have inherent limitations, a more efficient meshless method, known as peridynamics (PD), has been proposed and applied in various areas. PD has two types, namely, bond-based peridynamics (BPD) and state-based peridynamics (SPD). BPD is limited by its fixed Poisson's ratio, while SPD suffers from the zero-energy mode issue. A hybrid peridynamics (HPD) method is introduced in this paper to overcome these limitations, as it establishes bonds between each PD point and other PD points within its horizon and sums up all bond forces on the PD point to calculate the total force. The proposed HPD method is then applied to simulate three RC beams with different shear span-to-depth ratios. The simulation results, including the shear force–deflection of the beams, shear force–strain of stirrups, crack formation and propagation, and diagonal crack width, are compared against experimental data. The proposed HPD method is demonstrated as being capable of simulating RC structures' behaviors in an accurate and stable manner.

Keywords: peridynamics; reinforced concrete; zero-energy mode

Citation: Lin, C.; Lin, Z.; Xue, X.; He, S.; Wang, L. Refined Simulation of Reinforced Concrete Beam Based on a Hybrid Peridynamic Method.

Buildings **2023**, *13*, 1876. <https://doi.org/10.3390/buildings13071876>

Academic Editor: Elena Ferretti

Received: 25 April 2023

Revised: 23 June 2023

Accepted: 19 July 2023

Published: 24 July 2023



Copyright: © 2023 by the authors. Licensee MDPI, Basel, Switzerland. This article is an open access article distributed under the terms and conditions of the Creative Commons Attribution (CC BY) license (<https://creativecommons.org/licenses/by/4.0/>).

1. Introduction

The destruction and collapse of reinforced concrete (RC) structures under earthquakes may cause heavy casualties and economic losses. It is of great significance to study the failure mechanism of RC structures during earthquake excitation, including the generation and propagation of cracks, and the destruction of components. Among the currently used methods, the finite element method (FEM) is primarily effective in simulating the macroscopic mechanical behaviors of structures but faces challenges in accurately capturing discontinuous displacement fields and the evolution of cracks [1,2]; the discrete element method (DEM), a mesoscopic simulation method used to model the discontinuous behaviors of materials, often involves a large amount of computation and may present challenges when being applied to practical engineering problems [3,4].

Peridynamics (PD) is a meshless method capable of simulating the damage and fracture processes of materials, and which requires more time in general than FEM methods

but with accepted accuracy [5–7]. PD is a valuable choice for specific applications, and it is based on the concept of nonlocal interactions among PD points and their neighboring points, which naturally allows the capture of the formation and propagation of cracks. There are primarily two types of PD: the bond-based peridynamics (BPD) and the state-based peridynamics (SPD).

In the BPD method, one can calculate the bond force between a PD point and another point within its horizon based on the stretch of the bond. The direction of the bond force is assumed to align with the line connecting the two points; its magnitude can be computed using a one-dimensional (1D) constitutive model [7–9]. In civil engineering, BPD has been employed to investigate the damage, cracking, and failure behaviors of concrete structures. To give a few examples, Huang et al. used a refined BPD method to simulate the damage propagation and failure of concrete structures under tension, compression, and impact loading [10]. Demmie et al. performed simulations of the damage and failure behaviors of concrete structures under impact and explosive loads using BPD [11]. Zhang et al. developed a refined BPD model (i.e., an axial–shear interaction bond-slip model) for RC components and effectively simulated the damage behavior of RC, such as strength failure, stiffness degradation, crack propagation, and shear slip between reinforcement and concrete [12]. Although BPD is capable of solving various problems, its Poisson’s ratio μ is fixed in an elastic case (in plane stress cases $\mu = 1/3$, and in plane strain and three-dimensional cases $\mu = 1/4$), and the plastic incompressibility cannot be considered [7,13].

On the other hand, SPD can overcome BPD’s limitations and has found extensive application in the fields of solid mechanics, fluid mechanics, and heat conduction [14–18]. Regarding civil engineering applications, Gu et al. studied the tension, compression, and damage behaviors of concrete through a 3D Cap plastic model and SPD [19]. Lu et al. used SPD to simulate the pull-out test for a 3D anchor bolt and investigate its failure mechanism [20]. Dong et al. employed an SPD-based meso-scale damage model to analyze the damage and failure characteristics of concrete [21]. However, there is currently insufficient utilization of SPD in the simulation of RC structures. In addition, the SPD may suffer from the so-called “zero-energy mode” (i.e., the predicted responses by SPD, such as displacements, stresses, and strains, may be inaccurate or have spatial oscillation) [5,22–25]. To mitigate the zero-energy mode, several solutions have been proposed in the literature. For example, Silling presented a stable correspondence material model by introducing an additional force state density between each PD point and all neighboring points [26]. Breitenfeld et al. developed a similar approach, utilizing the average displacement across all points within the horizon to establish an additional force state density [27]. Although these methods are capable of mitigating the zero-energy mode issue, their applicability to highly nonlinear models with damage remains questionable.

This paper introduces a stabilized hybrid peridynamic (HPD) method to suppress the zero-energy mode issue of SPD and ensure that the solutions obtained are accurate and stable. The proposed HPD method builds upon a previous peridynamic method developed by the authors. However, while the previous method shares similarities with the HPD method, there is a significant difference in the approach used to calculate the strain, and the previous one has not been applied to simulate reinforced concrete beams [28]. The proposed HPD method is successfully implemented in OpenSees, and applied to simulate the refined mechanical behaviors of RC beams with different shear span-to-depth ratios, based on published test results [29]. The simulated results, including the shear force–deflection of the beams, shear force–strain curve of stirrups, the formation and propagation of cracks, and width of the diagonal cracks, are all compared against the experiment results, which showed that the proposed HPD method is an accurate and stable approach for simulating the behaviors of RC structures.

The manuscript is organized as follows: Section 1 provides the background and an introduction to the research topic. Section 2 introduces the theory of peridynamics, including the theory of BPD (Section 2.1), the theory of SPD (Section 2.2), and the theory of the proposed HPD (Section 2.3). Section 3 focuses on numerical applications, encompassing

subsections such as the introduction of the experiment (Section 3.1), the peridynamic model of the RC beams (Section 3.2), and specific beam configurations with shear span-to-depth ratios of 1.5, 2.0, and 2.6, respectively (Sections 3.3–3.5). Section 4 presents the conclusions of the paper.

2. The Theory of Peridynamics

As shown in Figure 1, the PD model assumes that within the range of horizon H_X , each material point X interacts with other material points, one of them denoted as X' . The bond vector between points X and X' in the reference configuration (denoted as ξ) is defined as the vector connecting these points. The relative displacement between points X and X' is denoted as η , i.e., $\eta = u' - u$. Consequently, in the deformed configuration, the relative position of points x and x' can be represented as the vector $\xi + \eta$.

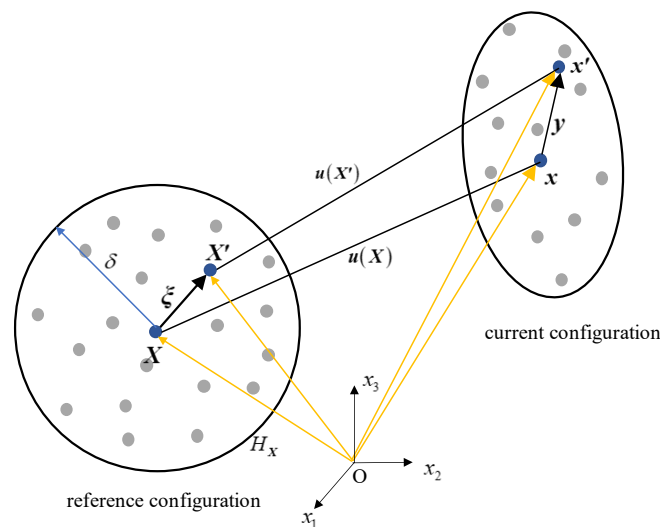


Figure 1. Deformation of points in PD.

Applying Newton's Second Law, the equation of motion for the material point X at time t can be expressed as follows [7],

$$\rho \ddot{u}(X, t) = L(X, t) + b(X, t) \quad (1)$$

where ρ is the mass density, \ddot{u} represents the acceleration of PD point X , b denotes the body force density, and $L(X, t)$ is the internal force on X . Depending on the format of $L(X, t)$, the three types of PD (i.e., BPD, SPD, and HPD) are elaborated in the subsequent sections.

2.1. BPD Theory

In BPD, $L(X, t)$ takes the form of:

$$L(X, t) = \int_{H_X} f(u' - u, X' - X, t) dV_{X'} \quad (2)$$

where $f(u' - u, X' - X, t)$ represents the pairwise force function between PD points X and X' , which can also be written as

$$f(u' - u, X' - X, t) = f(s)n \quad (3)$$

where n is the direction vector of the bond, and $f(s)$ is the magnitude of the bond force in the form of a function of bond stretch s , i.e.,

$$s = \frac{|\xi + \eta| - |\xi|}{|\xi|} \quad (4)$$

where $|\xi + \eta|$ and $|\xi|$ are the length of bond in the reference and deformed configurations, respectively. BPD is a straightforward and practical approach widely employed to address discontinuous problems. However, BPD is only suitable for 1D material constitutive models and not compatible with 3D ones. Additionally, BPD is incapable of taking the plastic volume incompressibility into consideration. In the case of elastic models, the Poisson's ratio μ is fixed in plane stress cases ($\mu = 1/3$) and in plane strain and 3D cases ($\mu = 1/4$).

2.2. SPD Theory

The equation of motion for SPD has the same format as Equation (1), while the second term $L(X, t)$ can be written as [30]:

$$L(X, t) = \int_{H_X} (\underline{T}(X, t) \langle \xi \rangle - \underline{T}(X', t) \langle -\xi \rangle) dV_{X'} \quad (5)$$

where $\underline{T}(X, t) \langle \xi \rangle$ and $\underline{T}(X', t) \langle -\xi \rangle$ are the force states as depicted in Figure 2. Specifically, $\underline{T}(X, t) \langle \xi \rangle$ is the force state of point X operating on ξ , and $\underline{T}(X', t) \langle -\xi \rangle$ shows that of point X' operating on $-\xi$.

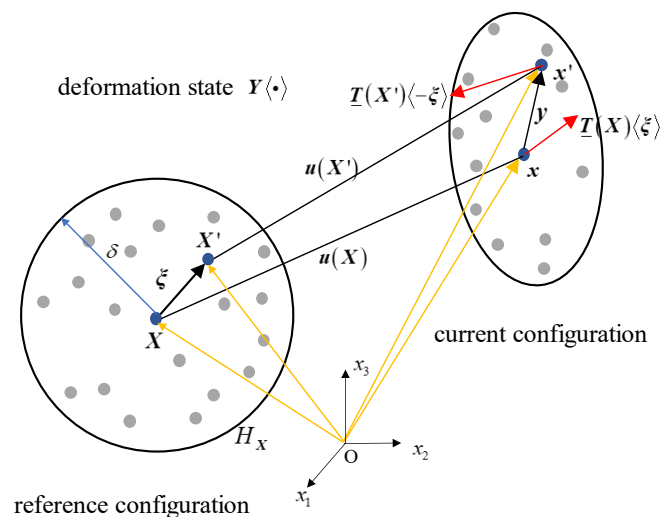


Figure 2. The deformation in SPD.

To calculate the force state of PD point X , the shape tensors in the reference and deformed configurations, $K(X)$ and $N(X)$, respectively, are calculated as follows:

$$K(X) = \int_{H_X} \underline{w} \langle \xi \rangle (\xi \otimes \xi) dV_{X'} \quad (6)$$

$$N(X) = \int_{H_X} \underline{w} \langle \xi \rangle (y \otimes \xi) dV_{X'} \quad (7)$$

where the symbol \otimes denotes the dyadic product of two vectors, y is the relative position of X and X' in current configuration, and \underline{w} is the influence function.

The deformation gradient $F(X)$ is calculated as

$$F(X) = N(X)K^{-1}(X) \quad (8)$$

Based on the virtual work principle, the force state $\underline{T}(X) \langle \xi \rangle$ in Equation (5) can be derived as [30]

$$\underline{T}(X) \langle \xi \rangle = \underline{w} \langle \xi \rangle P(X) K^{-1}(X) \xi \quad (9)$$

where $P(X)$ is the first Piola–Kirchhoff stress of point X transformed by the Cauchy stress $\sigma(X)$, which can be calculated by applying the constitutive law according to the strain $\epsilon(X)$,

and $\varepsilon(\mathbf{X})$ is obtained by the deformation gradient $\mathbf{F}(\mathbf{X})$ (according to the strain theory in continuum mechanics).

SPD is capable of overcoming the disadvantages of BPD and is widely used in various practical areas. However, SPD is susceptible to a phenomenon known as the “zero-energy mode,” which leads to notable challenges in terms of solution accuracy and stability. The root cause of the zero-energy mode lies in the approximation method of the deformation gradient at a PD point (i.e., the Equations (7)–(9)). The displacements of all neighboring points within its horizon are used when calculating the deformation gradient, which constitutes a homogenization process. Meanwhile, due to the potential presence of numerous neighboring PD points, such a homogenization process leads to a weak dependence of each bond's force density on its own stretch.

2.3. Hybrid Peridynamic Method

To address the limitations of BPD and SPD (more importantly, the zero-energy mode problem in SPD), a novel hybrid peridynamic method (HPD) is proposed. As with BPD, the HPD creates bonds between each PD point and its neighboring PD points within its horizon and calculates the total force on the PD point from all bond forces [28]. The equilibrium equation for HPD follows the same format as BPD and SPD (i.e., Equation (1)), and the computation of the pairwise force function $\mathbf{L}(\mathbf{X}, t)$ can also be computed using Equation (2). However, it is noteworthy that the direction of the pairwise force is not necessarily aligned with the bond, i.e.,

$$\mathbf{L}(\mathbf{X}, t) = \int_{H_X} \mathbf{f}(\mathbf{u}' - \mathbf{u}, \mathbf{X}' - \mathbf{X}, t) dV_{X'} \quad (10)$$

When HPD method is applied to 2D or 3D material constitutive models, the pairwise force $\mathbf{f}(\mathbf{u}' - \mathbf{u}, \mathbf{X}' - \mathbf{X}, t)$ is defined as the force at the cross-section at the midpoint of the bond. As shown in Figure 3, f_b is the pairwise force of point b , and is calculated by the 2D/3D stress tensor σ_b multiplied by the direction \mathbf{n} and the area A of the bond, i.e.,

$$f_b = \omega\langle\boldsymbol{\xi}\rangle \cdot \sigma_b \cdot \mathbf{n}_b \cdot A \quad (11)$$

where $\omega\langle\boldsymbol{\xi}\rangle$ is the influence state whose magnitude is related to the length of the bond and horizon size δ , and it is calculated as follows:

$$\omega\langle\boldsymbol{\xi}\rangle = \left(1 - \frac{|\boldsymbol{\xi} + \boldsymbol{\eta}|}{\delta}\right) \frac{g}{V_X V_{X'}} \quad (12)$$

where g is a variable related to the horizon size, V_X and $V_{X'}$ are the volume of PD point \mathbf{X} and \mathbf{X}' , respectively. In Equation (11), σ_b can be calculated by:

$$\sigma_b = \sigma_b(\varepsilon_b) \quad (13)$$

where ε_b is the strain tensor, which can be obtained by using the following equation,

$$\varepsilon_b = \frac{1}{2} \left(\mathbf{F}_b^T + \mathbf{F}_b \right) - \mathbf{I} \quad (14)$$

where \mathbf{F}_b is deformation gradient of point b , and \mathbf{I} is the identity matrix. \mathbf{F}_b is obtained using the following process.

As shown in Figure 4a, with \mathbf{X} as the endpoint and bond \mathbf{XX}' as the reference direction, the bonds with the smallest absolute angle relative to bond \mathbf{XX}' are searched in both clockwise and counterclockwise directions within the horizon of \mathbf{X} (assuming the counterclockwise rotation is positive). It is clear that bonds \mathbf{XB} and \mathbf{XD} have the smallest angles relative to bond \mathbf{XX}' ; thus, bond \mathbf{BD} can be determined as one of the virtual bonds for calculating the deformation gradient at point b . Additionally, as shown in Figure 4b, with \mathbf{X}' as the endpoint and $\mathbf{X'X}$ as the reference direction, bonds $\mathbf{X'A}$ and $\mathbf{X'E}$ have the smallest angles relative to $\mathbf{X'X}$; thus, bond \mathbf{AE} can be considered as another virtual bond

for obtaining the deformation gradient at point b . Ultimately, the deformation gradient at point b can be determined by bonds XX' , BD , and AE . Specially, the method to determine the deformation gradient of point b in cases where the numerical models are uniformly arranged can be referenced in Appendix A. Similar to SPD, the deformation gradient at point b in HPD can be calculated using the following equation,

$$F_b = N_b K_b^{-1} \quad (15)$$

where

$$K_b = \xi_{XX'} \otimes \xi_{XX'} + \xi_{BD} \otimes \xi_{BD} + \xi_{AE} \otimes \xi_{AE} \quad (16)$$

and

$$N_b = y_{XX'} \otimes \xi_{XX'} + y_{BD} \otimes \xi_{BD} + y_{AE} \otimes \xi_{AE} \quad (17)$$

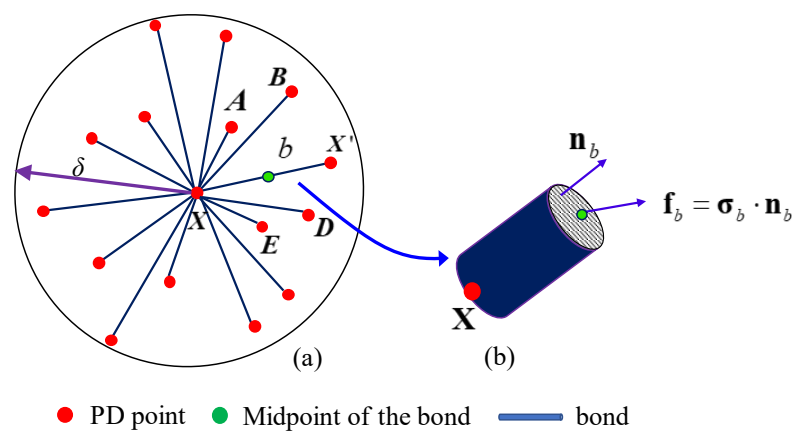


Figure 3. Deformation and the section view in HPD.

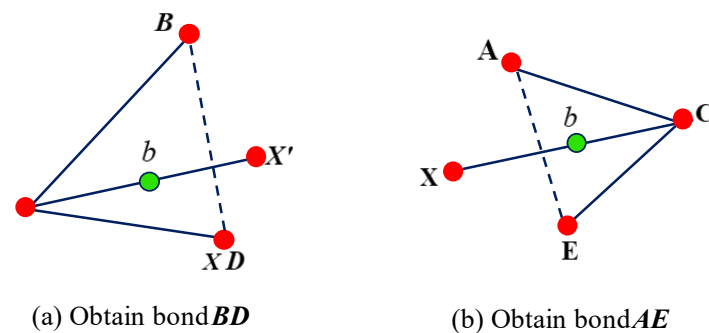


Figure 4. The method to obtain the deformation gradient of point b .

By performing the same calculations for all virtual bonds within the horizon of point X as with bond XX' , the forces exerted on point X (the first term on the right side of Equation (1)) can be obtained, and the equilibrium equation can be solved using Newton's second law or another explicit method. In this paper, the equilibrium equation of HPD is expanded into a form that can be applied to explicit and implicit integration methods for both static and dynamic analyses. Define the force density vector of PD point X as

$$r(X) = -L(X) \quad (18)$$

and Equation (1) can be rewritten as

$$\rho \ddot{u}(X) + r(X) = b(X) \quad (19)$$

Suppose $m(X) = \int_{V_X} \rho dV_X$, $\tilde{R}(X) = \int_{V_X} r(X) dV_X$, and $\tilde{b}(X) = \int_{V_X} b(X) dV_X$, and Equation (19) can be rewritten as

$$m(X)\ddot{u}(X) + \tilde{R}(X) = \tilde{b}(X) \quad (20)$$

Equation (20) is the equilibrium of PD point X . By listing and assembling the equilibrium equations for all PD points in the model and defining lumped mass matrix $M = \mathbf{A}_X(m(X))$, resisting force vector $R = \mathbf{A}_X(\tilde{R}(X))$, and external force vector $F = \mathbf{A}_X(\tilde{b}(X))$, the equilibrium equation of the PD model can be formed in the matrix and vector format as follows:

$$M\ddot{u} + R = F \quad (21)$$

Both explicit and implicit integration methods can be employed to solve Equation (20). In the context of this paper, an implicit method called Newton–Raphson iterative method is adopted for solving the equilibrium equation, unless otherwise specified. For static analysis, the first item $M\ddot{u}$ can be omitted.

The proposed HPD method presented herein has been implemented in OpenSees, an open-source finite element framework widely used for various nonlinear problems, especially in the field of civil engineering.

3. Applications

3.1. Introduction of the Experiment

Numerical simulations were conducted on three RC beams with different shear span-to-depth ratios, and the results were compared with experiment results obtained in test measurements [29,31]. The experimental model of the beam is shown in Figure 5.

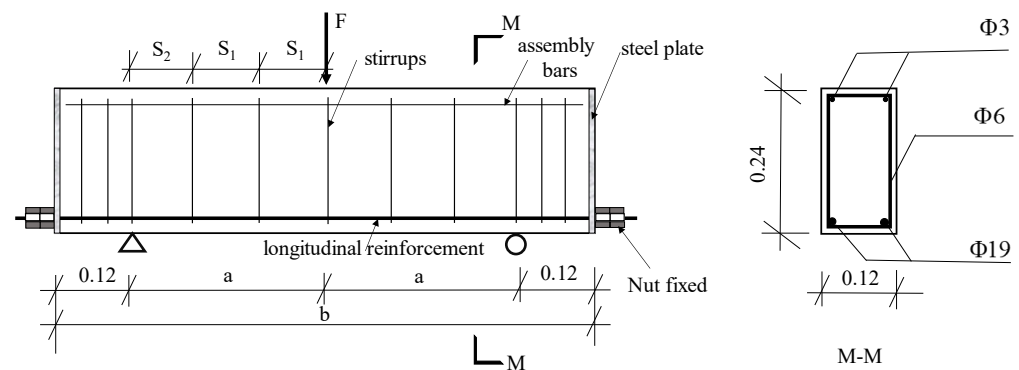


Figure 5. The experimental model of the beam.

The shear span-to-depth ratios of the three RC beams are 1.5, 2.0, and 2.6, respectively. All three beams have the same cross-sectional dimensions, with a width of 0.12 m, a height (depth) of 0.24 m, and an effective section height of 0.22 m. The shear span-to-depth ratio is represented by $\lambda = \frac{a}{d}$. The geometric parameters of the beams are presented in Table 1, where the number following “BEAM” indicates the magnitude of the shear span-to-depth ratio. b denotes the total length of the beam, while S1 and S2 represent the spacings between adjacent stirrups.

In the experiment, longitudinal reinforcement in the RC beams was provided by 19 mm diameter high-strength deformed bars with a yield strength of 708 MPa. Three-millimeter-diameter steel wires were placed in the top section zone as assembly bars, while stirrups were fabricated from 6 mm diameter plane round steel bars with a yield strength of 300 MPa. After the specimen was prepared, a three-point bending test was carried out and the loading process was displacement-controlled with an increment of 0.2 mm/min.

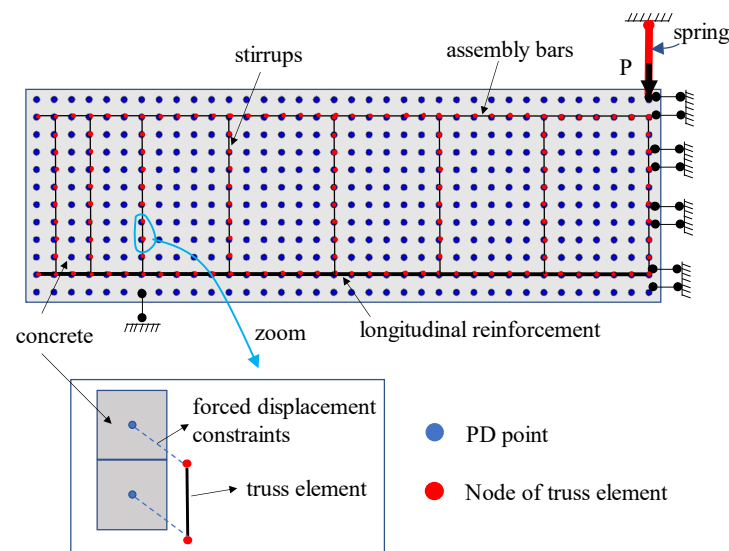
Table 1. The geometric parameters of the beams with different shear span-to-depth ratios.

ID	Shear Span-to-Depth Ratio	<i>a</i> (m)	<i>b</i> (m)	S1 (m)	S2 (m)
BEAM1.5	1.5	0.33	0.9	0.12	0.09
BEAM2.0	2.0	0.44	1.12	0.12	0.08
BEAM2.6	2.6	0.58	1.4	0.12	0.1

3.2. The PD Model of the RC Beams

3.2.1. The Geometric Model

The proposed HPD method was used to perform static analysis on RC beams with different shear span-to-depth ratios. In the following context, “PD” refers to the HPD method. Due to the symmetry of the geometry and loading conditions of the RC beams, a half-span structure is used for simulation. Taking the case of BEAM2.6 as an example, the numerical model is shown in Figure 6:

**Figure 6.** Numerical model of the RC beam.

PD and FEM models are used to simulate the mechanical behaviors of concrete and steel reinforcement, respectively. The concrete is discretized into a PD model that consists of PD material points, while the steel reinforcement is simulated using a finite element model (i.e., truss element). Shear slippage between the steel reinforcement and concrete is not considered, and the enforced displacement constraints are used between PD points and truss nodes. A hinge support is placed at the left bottom of the beam, and the node's degree of freedom (DOF) is fixed in the *y* direction, while being free in the *x* direction. A sliding support is used at the mid-span of the beam, whose nodal DOF is fixed in the *x* direction and free in the *y* direction. To simulate the displacement-controlled loading process, a spring with high elastic modulus is set at the top of the beam.

In the three numerical examples, the truncated Drucker–Prager model (TDP) is used to simulate the concrete material, while a bilinear model is employed for the steel reinforcement. TDP is an advanced constitutive model utilized to describe the nonlinear behavior of concrete.

3.2.2. The TDP Model

Figure 7 shows the TDP model, which has two yield surfaces, including the shear failure yield function (f_1) and tensile cutoff yield function (f_2). The shear failure yield function is defined as

$$f_1(\sigma) = \|s\| - F_e(I_1), \quad F_e(I_1) = \alpha + \lambda I_1 \quad (22)$$

where $\sigma = s + \left(\frac{1}{3}I_1\right)I_2$ is the stress tensor (I_2 is the second order identity tensor), s is the deviatoric stress component, and I_1 is the volumetric stress component. $\|s\|$ is the norm of the deviatoric stress tensor and $\|s\| = \sqrt{s:s}$, in which “:” is the dyadic tensor product. α is the shear strength when the volumetric stress is zero and λ is the slope of f_1 . The shear failure yield surface only considers material yielding caused by shear force.

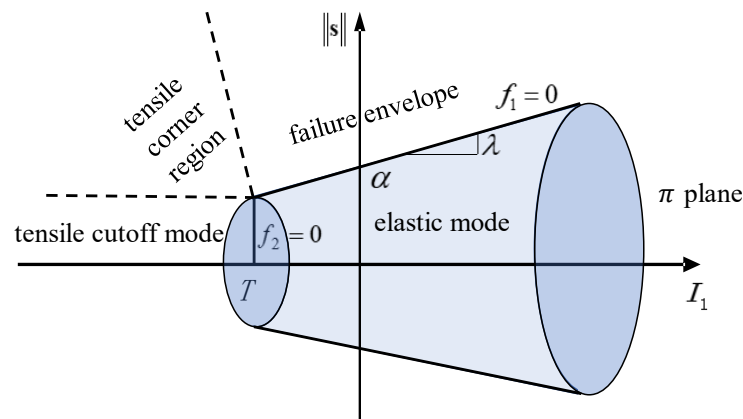


Figure 7. The TDP model.

The tensile cutoff yield function is defined as

$$f_2(\sigma) = T - I_1 \quad (23)$$

where T is the maximum hydrostatic tensile strength. The tensile cutoff yield surface only considers material yielding caused by tensile force.

The generalized associative flow rule of the TDP model is defined as

$$\dot{\epsilon}^p = \sum_{i=1}^2 \dot{\gamma}_i \frac{\partial f_i}{\partial \sigma} \quad (24)$$

where $\dot{\epsilon}^p$ is the plastic strain rate, $\dot{\gamma}_i$ is the magnitude of the plastic strain rate, and $\frac{\partial f_i}{\partial \sigma}$ is the direction of the plastic strain. According to the equation, the direction of $\dot{\epsilon}^p$ is assumed to be consistent with the outer normal direction of the yield surface.

From Figure 7, the two yield surfaces clearly divide the stress space into four sub-regions specified by four modes, i.e., tensile cutoff mode, tensile corner region, failure envelope mode, and elastic region. The elastic region is given by stress states such that $f_1(\sigma) < 0$ and $\dot{\gamma}_i = 0$. The stress computation algorithms are different for each mode, which is introduced in detail in the literature [32].

The material parameters used in the three examples are shown in Table 2, where ρ is the density of concrete, G is the shear modulus, and K is the bulk modulus.

Table 2. Material parameters in TDP model.

Material Parameters	ρ (t/m ³)	G (kPa)	K (kPa)	λ	α (kPa)	T (kPa)
	2400	1.64×10^7	1.22×10^7	0.3435	1.1×10^4	-1.43×10^3

3.2.3. The Bilinear Model

The bilinear model is particularly useful for simulating steel bars that exhibit elastic and plastic behaviors. The model is shown in Figure 8. The stress–strain relationship can be written as

$$\sigma = \begin{cases} E\varepsilon & \text{elastic} \\ \sigma_y + bE\left(\varepsilon - \frac{\sigma_y}{E}\right) & \text{plastic} \end{cases} \quad (25)$$

where σ and ε are the stress and strain, respectively; E , σ_y , and b are the elastic modulus, yield stress, and the ratio between the post-yield tangent and initial elastic tangent, respectively. The parameters of the longitude reinforcement, stirrups, and assembly bars used in the numerical examples are shown in Table 3.

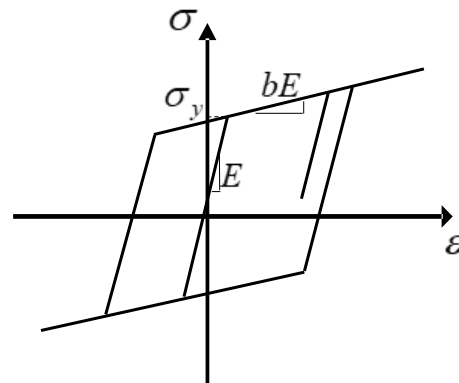


Figure 8. The bilinear model.

Table 3. The parameters of steel bars using bilinear model.

	E (kPa)	σ_y (kPa)	b
longitude reinforcement	2.482×10^8	7.06×10^5	0.02
assembly bars	2.482×10^8	3×10^5	0.02
stirrups	2.482×10^8	3×10^5	0.02

3.3. RC Beam with a Shear Span-to-Depth Ratio of 1.5

3.3.1. The Detailed Model of BEAM1.5

The model of BEAM1.5 is shown in Figure 9. The concrete model is divided into 23 columns and 12 rows, resulting in a total of 276 PD points. The grid size of the PD model is 0.02 m, and the volume of each PD point is 0.000048 m³; the plane strain condition is used here, and the thickness of the beam is 0.12 m. The radius of the horizon δ is set to be 0.3 m. The geometry and material parameters of the concrete and steel bars are provided in Section 3.2 and are therefore not repeated here.

A static analysis is performed for this example. The Newton–Raphson iterative method is used for solving the equilibrium equation $\mathbf{R}(\mathbf{u}) = \mathbf{B}$, and the norm of the incremental displacement vector is used as a convergence criterion with a tolerance of 10^{-6} m.

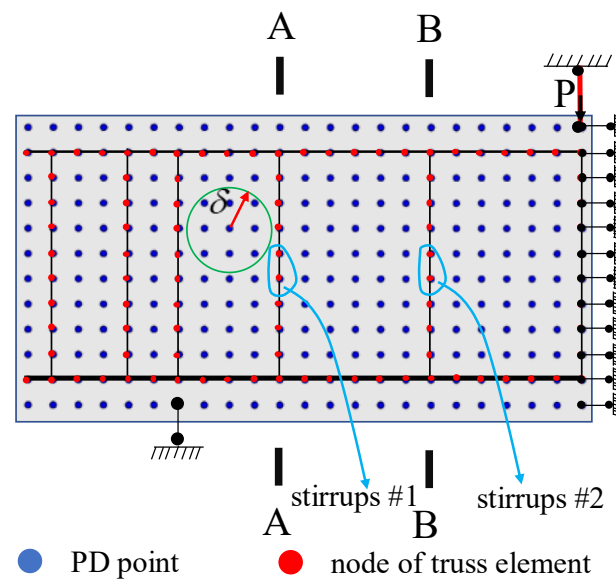


Figure 9. PD model of RC beam with a shear span-to-depth ratio of 1.5.

3.3.2. Comparison of Force–deflection Curve

Figure 10 shows the comparison of the force–deflection curve between the experiment and PD results for BEAM1.5. The horizontal axis represents the deflection of the beam, and the vertical axis represents the force exerted on the beam. The red solid line corresponds to the experimental results, while the blue dashed line represents the PD results. The results of the experiment and PD show good agreement, and the spatial oscillation of the PD points is virtually nonexistent. The peak force in the experiment is 216.6 kN, while the simulation result is 228.7 kN, resulting in an acceptable level of error at 5.6%.

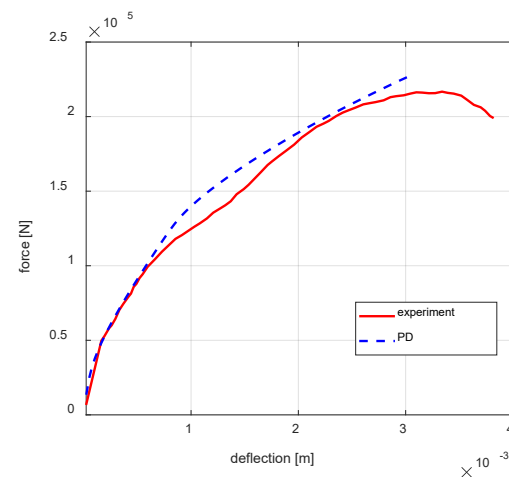


Figure 10. Comparison of force–deflection curve between experiment and PD results.

In the initial stage of the experiment, the incomplete compression of the loading pad and the uneven surface of the concrete may cause the beam stiffness to be far smaller than its actual value. Therefore, we moved the experimental curve to the left and modified the initial stiffness until it matched the actual initial stiffness of the concrete (the elastic modulus of C30 concrete in the elastic stage is 2.95×10^{10} Pa and the Poisson's ratio is 0.2, which can be used to calculate the approximate stiffness of the concrete). In the experiment, the stiffness of the beam decreases continuously with the increase in load (indicating that the beam gradually entered the plasticity stage), and the same trend is present in the PD results. From Figure 10, it is observed that after reaching the peak force, the experimental curve

shows a downward trend. However, this phenomenon was not applicable to the numerical simulation result (i.e., the load-bearing capacity of the PD model does not decrease after reaching the peak value). This may be attributed to the use of the TDP model for the concrete; since the shear failure yield surface of the TDP model cannot decrease and the maximum shear bearing capacity increases with the increase in the bulk stress, it cannot simulate the decrease in the load-bearing capacity of the RC beam.

3.3.3. Comparison of the Shear Force–Strain Curves for Stirrups

Figure 11 shows the comparison of the shear force–strain curves for stirrup #1 and stirrup #2 between the experiment and PD results in the BEAM1.5. The horizontal axis represents the strain of the stirrup, while the vertical axis represents the magnitude of the shear force acting on the stirrups. Solid lines represent the experimental results, while dashed lines represent the PD simulation results. Red lines show the results for stirrup #1, and blue lines show the results for stirrup #2. The results of the experiment and PD are in relatively good agreement: during the initial loading stage, the strain of the stirrup does not change significantly, indicating that no cracks have yet emerged at the stirrup location. As the load increases, shear cracks are generated near the supports and continue to grow. When the cracks pass through the stirrups, the strain gradually increases. With the continuous growth of diagonal cracks, the stress in the stirrups increases until yielding occurs.

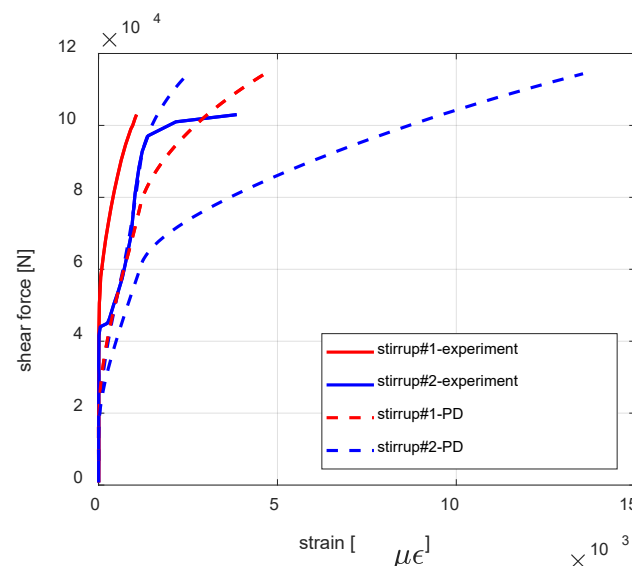


Figure 11. Comparison of shear force–strain curves of stirrups #1 and #2 between experiment and PD results.

3.3.4. Strain Distribution of Stirrups

Figure 12 shows the strain distribution of stirrups at sections A–A and B–B of the BEAM1.5. The purple area in the figure represents the actual crack location observed in the experiment. As the strain gauges were only attached at the middle of the cross-section of the beam during the experiment, only the numerical simulation results are discussed here. On the cross-section A–A, the strain of all segmented stirrups at the peak load can be calculated by drawing a horizontal solid black line corresponding to the magnitude of the strain. Connect these lines and the strain distribution of the stirrups can be obtained, which is represented by the portion indicated by the solid red line. The strain distribution of the stirrups on section B–B follows a similar approach. As can be seen from the figure, at the peak load, the stirrups near the bottom of section A–A have the largest strain, and the strain decreases continuously along the y direction; on section B–B, the upper-middle part of the stirrups has the largest strain, while the strains on both sides are smaller.

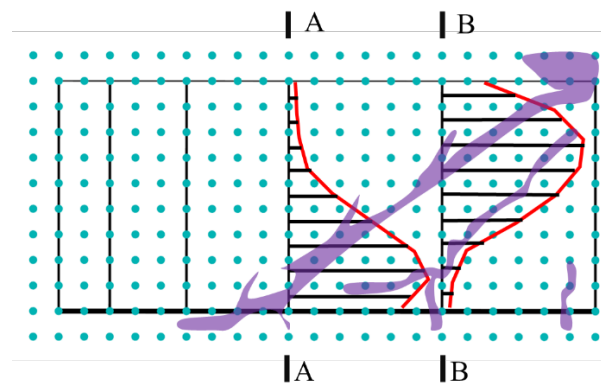


Figure 12. The strain distribution of stirrups at sections A–A and B–B.

3.3.5. Analysis of the Shear Crack

During the experiment, a shear crack appears near the support and grows as the load increases; when the crack passes through the stirrups, the strain on the stirrups increases rapidly. Therefore, the location with the largest stirrup strain is considered as the most prominent place for crack growth. By connecting the locations with the largest stirrup strain with a straight line, the position and direction of the main diagonal crack in the beam can be approximated.

In actual engineering circumstances, the tensile strength of concrete is relatively low, and the main cause of crack formation is tensile failure. Therefore, it is appropriate to determine the formation and expansion of cracks in RC beams based on the magnitude and direction of the principal tensile strain of the PD points. If the maximum principal strain is the principal tensile strain, a crack is formed at that point and the direction is perpendicular to the direction of the principal tensile strain. Figure 13 shows the diagonal crack pattern of the BEAM1.5 at the peak load, as Figure 13a,b show the results of the experiment and PD, respectively. The blue solid lines can be regarded as simulated cracks whose width and length represent the magnitude of the crack, and the directions are perpendicular to the principal tensile strain direction.

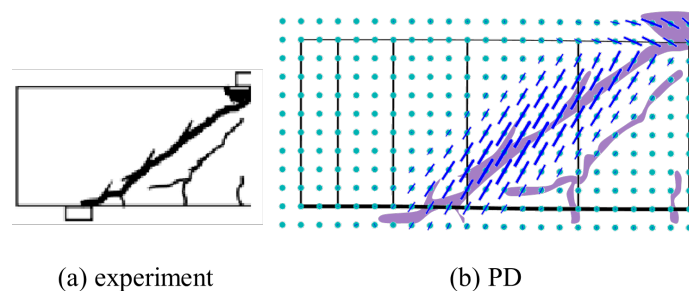


Figure 13. Comparison of the direction of crack.

The formation and propagation of cracks obtained using the principal tensile strain method can be considered as diffuse cracking. Although all cracks cannot practically be merged into one main crack, connecting the locations with the largest simulated strain of the stirrup using a straight line, the position and direction of the main diagonal crack in the beam can be approximated.

To compare the width of the crack, the following crack formula is used [33], i.e.,

$$d_c = g \times (\varepsilon_1 - \sigma_1 / E) \quad (26)$$

where d_c is the width of crack, g is the grid size (in PD model, g is dx), ε_1 and σ_1 are the first principle strain and first principle stress, respectively. E is the young's modulus of concrete ($E = 2.95 \times 10^{10}$ Pa). The crack width at each PD point is calculated, and all of the

crack widths on the M-M section are summarized to obtain the width of the diagonal crack. Figure 14 compares the predicted diagonal crack widths using PD and the experiment, and it shows that with the increase in loading, the diagonal crack width increases continuously. The relative error between PD and the experiment is small in the early loading stage but increases as the loading increases. Table 4 shows the detail of the width of the diagonal crack, the maximum relative error is 19.3% when the width of the crack is 0.25×10^{-4} m.

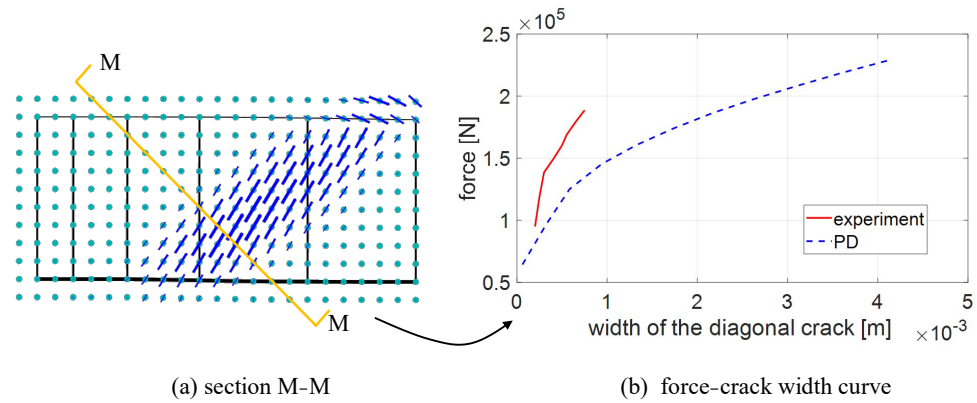


Figure 14. Comparison of the width of the diagonal crack.

Table 4. The detail of the width of the diagonal crack of BEAM1.5.

Width of Crack ($\times 10^{-4}$ [m])		0.25	0.3	0.4	0.5	0.55	0.65	0.75
Load ($\times 10^5$ (N))	Experiment	1.19	1.39	1.49	1.60	1.69	1.79	1.89
	HPD	1.42	1.51	1.67	1.81	1.88	2.00	2.12

3.4. RC Beam with a Shear Span-to-Depth Ratio of 2.0

3.4.1. The Detail Model of BEAM2.0

The model of BEAM2.0 is shown in Figure 15. The concrete model is divided into 29 columns and 12 rows, resulting in a total of 348 PD points. The geometric and material parameters are the same with the RC beam shown in Section 3.3. A static analysis is performed. The Newton–Raphson iterative method is used for solving the equilibrium equation, and the norm of the incremental displacement vector is used as a convergence criterion with a tolerance of 10^{-6} m.

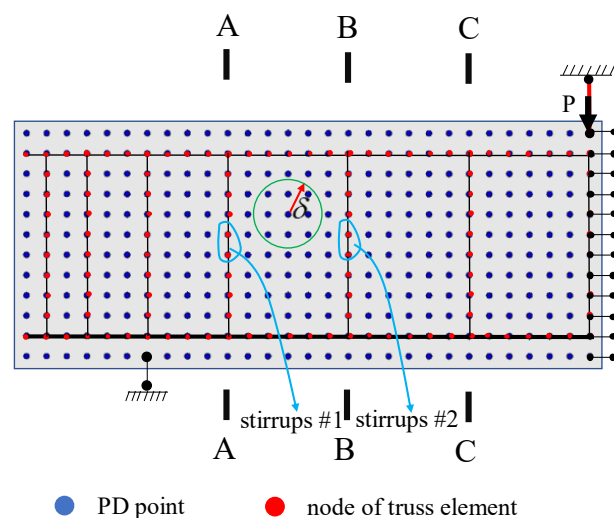


Figure 15. PD model of RC beam with a shear span-to-depth ratio of 2.0.

3.4.2. Comparison of Force–deflection Curve

Figure 16 shows the comparison of the force–deflection curve between the experiment and PD results for BEAM2.0. The horizontal axis represents the deflection of the beam, while the vertical axis represents the force acting on the concrete beam. The red solid line corresponds to the experimental results, while the blue dashed line represents the PD results. The experimental data were processed in the same manner as described in Section 3.3. The results of the experiment and PD show good agreement. The peak force in the experiment is 163.5 kN and the simulation result is 158.4 kN, resulting in a relative error of 3.1%. However, from Figure 16, the load-bearing capacity of the PD model does not decrease after reaching the peak value. This is for the same reason as described in Section 3.3.

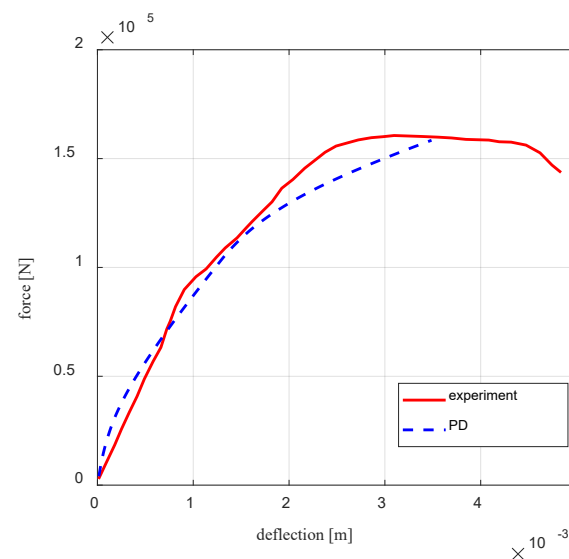


Figure 16. Comparison of force–deflection curve between experiment and PD results.

3.4.3. Comparison of the Shear Force–strain Curves for Stirrups

Figure 17 shows the comparison of the shear force–strain curves for stirrup #1 and stirrup #2 between the experiment and PD results in the BEAM2.0. The horizontal axis represents the strain of the stirrup, and the vertical axis represents the magnitude of the shear force exerted on the stirrups. Solid lines represent the experimental results, while dashed lines represent PD simulation results. Red lines show the results for stirrup #1, and blue lines show the results for stirrup #2. The trends of the experimental results and PD results are in relatively good agreement. In the initial loading stage, the strains of the stirrup using PD are consistent with the experiment; however, as the load increases, especially when the structure enters the plastic stage, the relative errors between PD and the experiment become larger.

3.4.4. Strain Distribution of Stirrups

Figure 18 shows the strain distribution of the stirrups at sections A–A, B–B, and C–C of the BEAM2.0. As can be seen from the figure, at the peak load, the stirrups near the bottom of section A–A have the largest strain; on section B–B, the middle part of the stirrups has the largest strain; and on section C–C, the upper-middle part of the stirrups has the largest strain. Similar to the case of BEAM1.5, by connecting the points of the maximum stirrup strain with a straight line, the approximate location and direction of the main diagonal crack in the beam can be simulated.

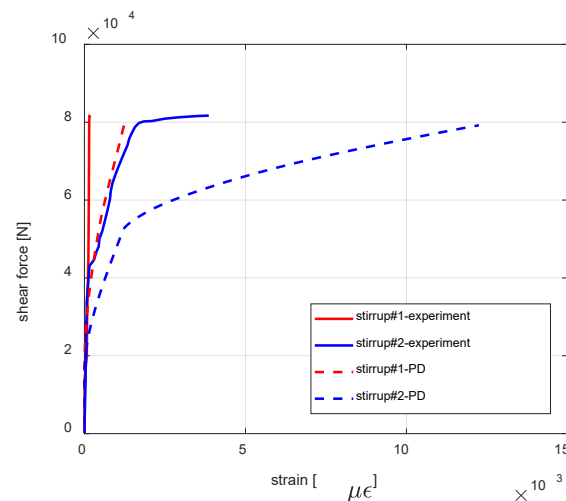


Figure 17. Comparison of shear force–strain curves of stirrups #1 and #2 between experiment and PD results.

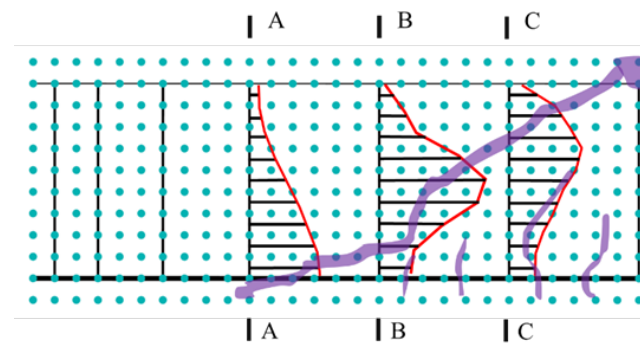


Figure 18. The strain distribution of stirrups at sections A–A, B–B, and C–C.

3.4.5. Analysis of the Shear Crack

The method used in Section 3.3 is employed to analyze the crack width and direction of BEAM2.0. Figure 19a,b display the crack of BEAM2.0 using the experiment and PD, respectively. In Figure 19b, the blue solid line can be considered as the crack predicted by PD, with its width and length representing the magnitude of the crack, and its direction is perpendicular to the principal tensile strain. The purple area in the figure indicates the crack in the experiment. It can be observed that a horizontal crack appears at the top of the beam; in addition, the straight line connecting the locations of the largest simulated cracks matches well with the actual crack. The crack width of the diagonal cracks is calculated using the same method as in Section 3.3. As shown in Figure 20, the predicted diagonal crack width using PD and the experiment are compared, and the results are in good agreement. Table 5 shows the detail of the width of the diagonal crack, and the maximum relative error is 10% when the width of the crack is 0.96×10^{-4} m.

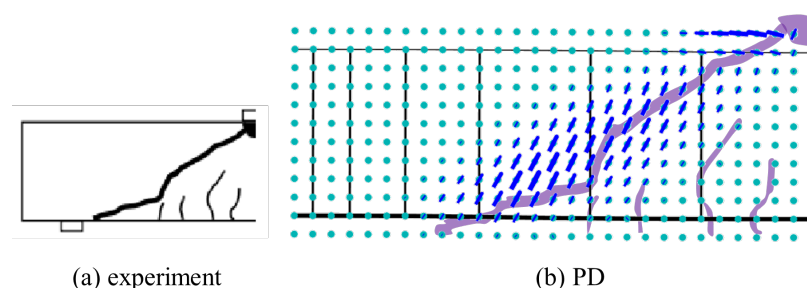


Figure 19. Comparison of the direction of crack for BEAM2.0.

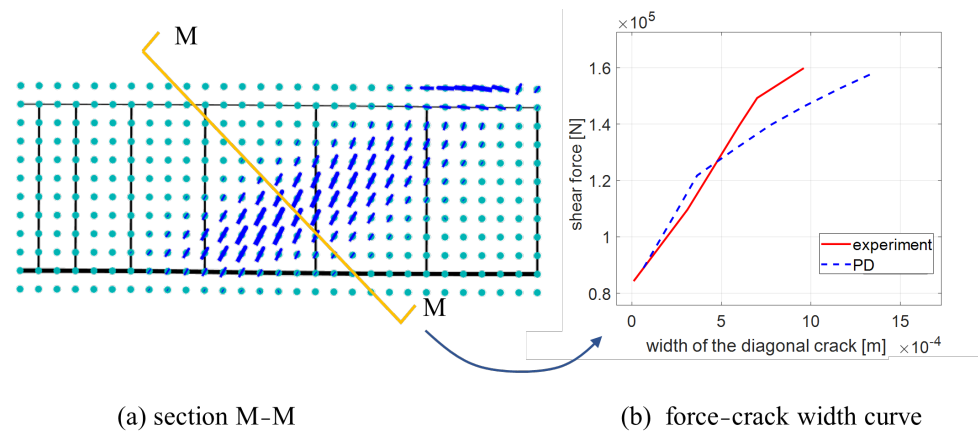


Figure 20. Comparison of the width of the diagonal crack for BEAM2.0.

Table 5. The detail of the width of the diagonal crack for BEAM2.0.

Width of Crack ($\times 10^{-4}$ [m])		0.01	0.31	0.51	0.6	0.7	0.96
Load ($\times 10^5$ (N))	Experiment	0.84	1.10	1.30	1.40	1.49	1.6
	HPD	0.88	1.15	1.26	1.31	1.35	1.44

3.5. RC Beam with a Shear Span-to-Depth Ratio of 2.6

3.5.1. The Detailed Model of BEAM2.6

The model of BEAM2.6 is shown in Figure 21. The concrete model is divided into 36 columns and 12 rows, resulting in a total of 432 PD points. Other geometric and material parameters are the same as those for the RC beam shown in Sections 3.3 and 3.4. The static analysis is performed. The Newton–Raphson iterative method is used for solving the equilibrium equation, and the norm of the incremental displacement vector is used as a convergence criterion with a tolerance of 10^{-6} m.

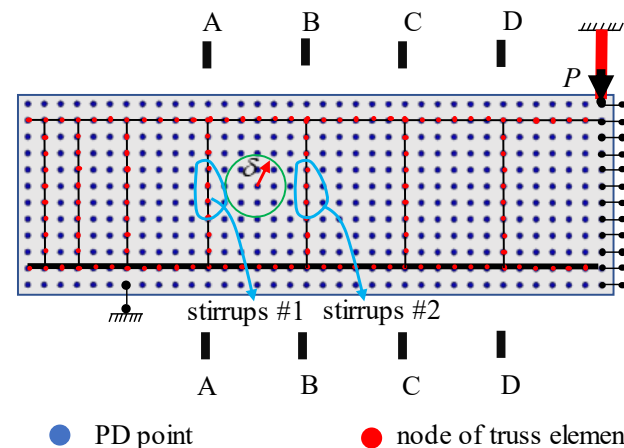


Figure 21. PD model of RC beam with a shear span-to-depth ratio of 2.6.

3.5.2. Comparison of Force–deflection Curve

Figure 22 shows the comparison of the force–deflection curve between the experiment and PD results for BEAM2.6. The experimental data were processed in the same manner as described in Sections 3.3 and 3.4. The results of the experiment and PD show good agreement. The peak force in the experiment is 147.6 kN and the simulation result is 143.6 kN, resulting in a relative error of 2.7%. From Figure 22, the load-bearing capacity of the PD model does not decrease after reaching the peak value for the same reason as described in Section 3.3.

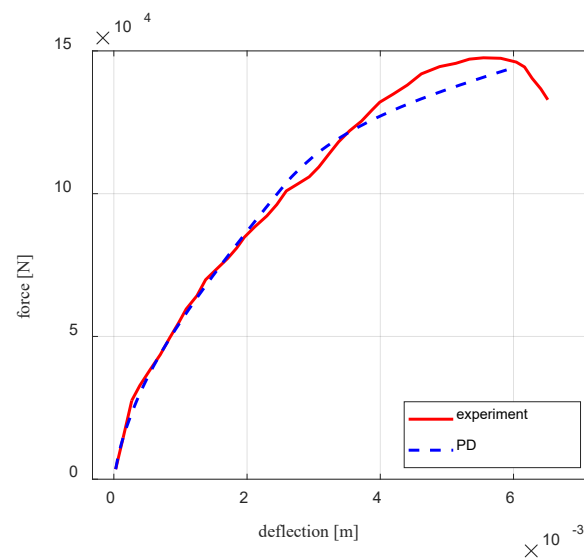


Figure 22. Comparison of shear force–deflection curve between experiment and PD results.

3.5.3. Comparison of the Shear Force–strain Curves for Stirrups

Figure 23 shows the comparison of the shear force–strain curves for stirrup #1 and stirrup #2 between the experiment and PD results in the BEAM2.6. The trends of the experimental results and PD results are in relatively good agreement.

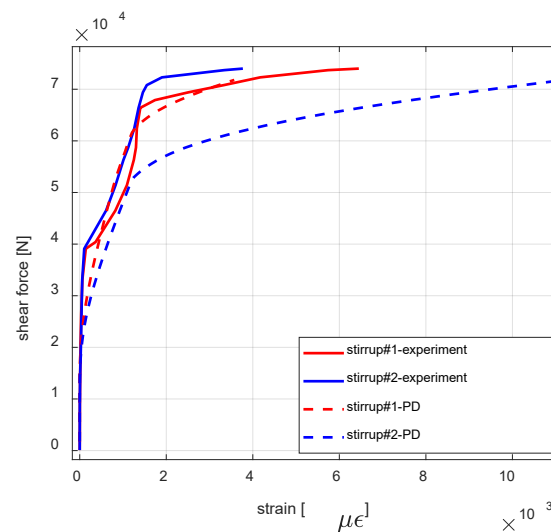


Figure 23. Comparison of shear force–strain curve of stirrups #1 and #2 between experiment and PD results.

3.5.4. Strain Distribution of Stirrups

Figure 24 shows the strain distribution of stirrups at sections A–A, B–B, C–C, and D–D of the BEAM2.6. As can be seen from the figure, at the peak load, the stirrups near the bottom of section A–A have the largest strain; on section B–B, the middle part of the stirrups has the largest strain; on section C–C, the upper-middle part of the stirrups has the largest strain; and on section D–D, the top of the stirrups has the largest strain. Similar to the cases of BEAM1.5 and BEAM2.0, connecting the points of the maximum stirrup strain with a straight line yields the approximate location and direction of the main diagonal crack.

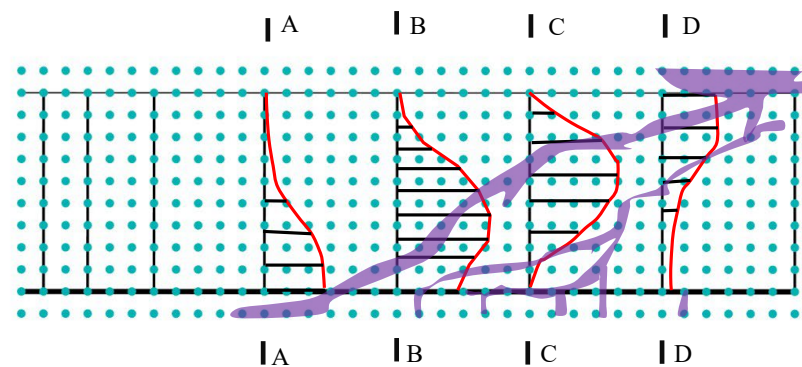


Figure 24. The strain distribution of stirrups at sections A–A, B–B, and C–C.

3.5.5. Analysis of the Shear Crack

The method used in Section 3.4 is employed to analyze the crack width and direction of BEAM2.0. Figure 25b uses the same configuration as Figure 19b and the observations are also similar between BEAM2.0 and BEAM2.6, which is also true for Figures 20 and 26. In sum, the results of BEAM2.6 from the experiment and PD are in good agreement as well. Table 6 shows the detail of the width of the diagonal crack, and the maximum relative error is 6% when the width of the crack is 0.55×10^{-4} m.

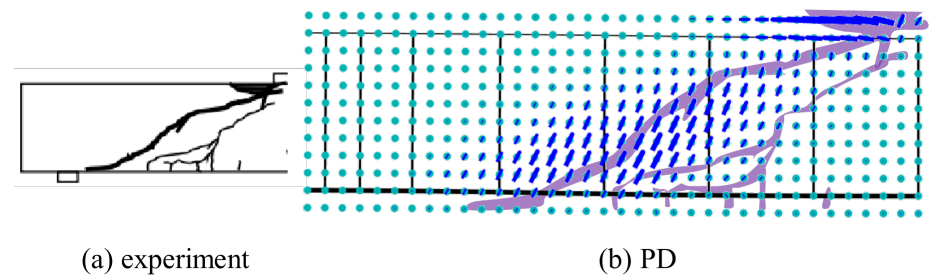


Figure 25. Comparison of the direction of crack for BEAM2.6.

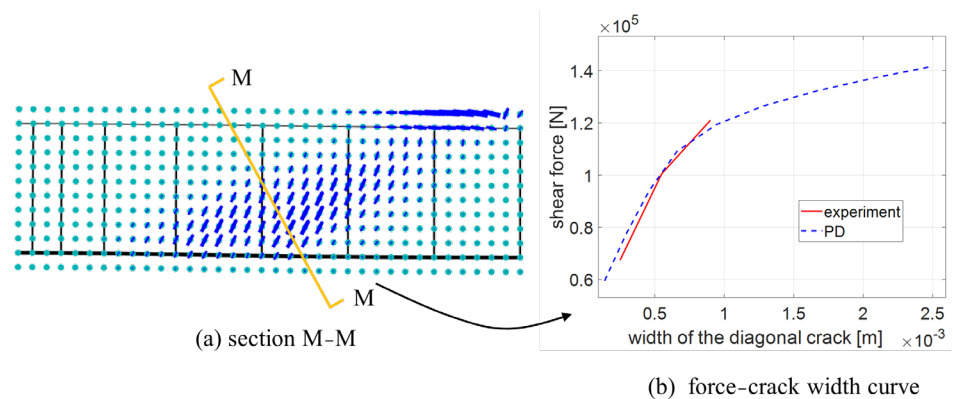


Figure 26. Comparison of the width of the diagonal crack for BEAM2.6.

Table 6. The detail of the width of the diagonal crack for BEAM2.6.

Width of Crack ($\times 10^{-4}$ [m])		0.25	0.55	0.90
Load ($\times 10^5$ [m]N)	Experiment	0.67	1.0	1.21
	HPD	0.67	0.94	1.18

4. Conclusions

This paper introduces a stabilized hybrid PD method (HPD) to simulate the mechanical behaviors of reinforced concrete (RC) beams. HPD uses a similar equation of motion as that of bond-based peridynamics, as the internal force is also calculated based on all bond forces within its horizon. What is different for HPD is that the bond forces are determined by using the stress tensor at the midpoint of the bond, multiplied by the direction and area of the bond. The stress tensor is calculated using two- or three-dimensional material constitutive models based on the strain at the bond's midpoint. The strain is obtained by using a similar homogenization method to that in SPD.

Three examples of RC beams with different shear span-to-depth ratios are presented herein to verify the accuracy and stability of the proposed HPD method in terms of its ability to simulate the mechanical behaviors of RC beams, including the shear force–deflection of the beams, shear force–strain curve of stirrups, crack formation and propagation, and the diagonal crack width of the beam. The HPD results are relatively consistent with those of the experiment and no zero-energy mode in SPD is present, which shows that the proposed HPD method is a practical and effective alternative to solve complex problems of RC structures.

Author Contributions: Conceptualization, C.L., Z.L. and L.W.; writing—original draft preparation, L.W.; writing—review and editing, S.H., X.X. and C.L.; investigation, X.X.; visualization, S.H.; funding acquisition, L.W. All authors have read and agreed to the published version of the manuscript.

Funding: This research was funded by the Science and Technology Plan Project of Wenzhou, China (grant. No. S20220004).

Data Availability Statement: Not applicable.

Conflicts of Interest: The authors declare no conflict of interest.

Appendix A

In this paper, all the numerical models are uniformly arranged. The coefficient g in Equation (12) can be obtained through an inverse calculation algorithm. When $\delta = 1.5dx$, the value is 2.40. The cross-sectional area of the bond is $A = dx \cdot t$, where t represents the width of the cross-section (i.e., the thickness of the two-dimensional model).

The following section provides a detailed explanation of the method for solving the deformation gradient at the midpoint of the virtual bond.

As shown in Figure A1, the red points represent the PD points, the solid blue line represents the bond, and the green point b represents the midpoint of the bond XC . To calculate the deformation gradient at point b , according to the calculation method of HPD, set point X as the endpoint and XC as the reference direction, and find the two bonds (light blue dashed lines) with the smallest absolute angle with XC . In this example, they are XD and XB , with angles $+45^\circ$ and -45° with respect to XC , respectively. Thus, the bond BD is selected as one of the bonds to approximate the deformation gradient at point b (see Figure A1a). Then, considering point C as the endpoint and direction CX as the reference direction, CA and CE are the two bonds with the smallest absolute angle with CX . Therefore, AE is selected as another bond to approximate the deformation gradient at point b (see Figure A1b). Finally, the deformation gradient at point b can be approximated by using the bonds XC , AE , and BD with Equation (12) (see Figure A1c).

For the inclined bond XB shown in Figure A2, the calculation of the deformation gradient at point b is similar to that of the horizontal bond. The difference lies in the selection of the bonds when approximating the strain of point b . With X as the endpoint and XB as the reference direction, the bond AC is selected (see Figure A2a). When considering point B as the endpoint and BX as the reference direction, the bond AC is selected (see Figure A2b). Therefore, only the bonds XB and AC are needed to approximate the deformation gradient at the midpoint b of the inclined bond XB (see Figure A2c).

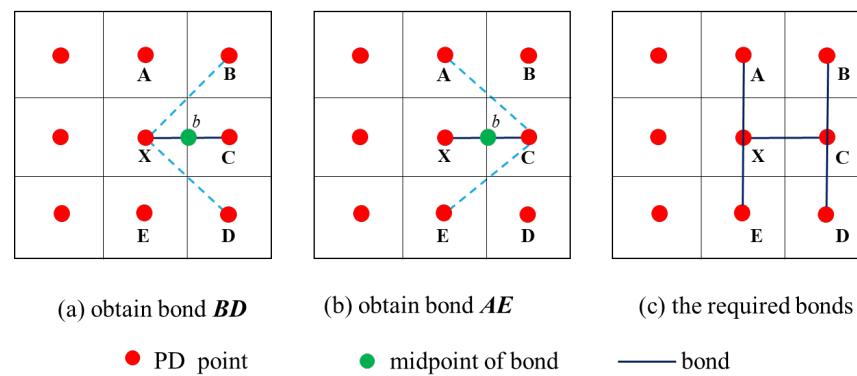


Figure A1. The deformation gradient of the midpoint b of the horizontal bond.

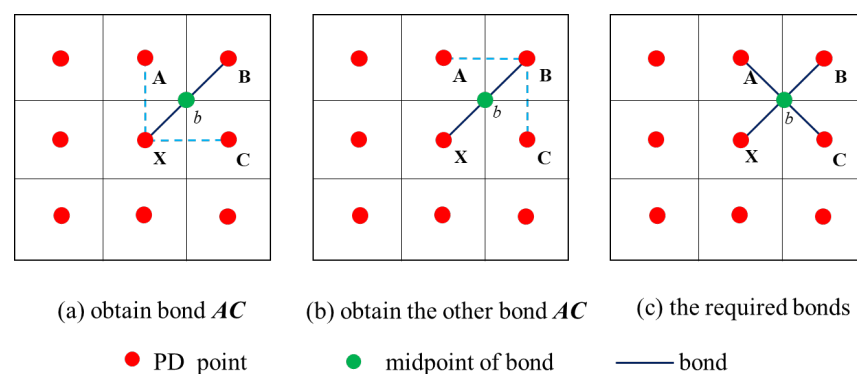


Figure A2. The deformation gradient of the midpoint b of the inclined bond.

References

- Łodygowski, T.; Sumelka, W. Limitations in application of finite element method in acoustic numerical simulation. *J. Theor. Appl. Mech.* **2006**, *44*, 849–865.
- Nwanoro, K.C.; Lu, H.; Yin, C.; Bailey, C. Advantages of the extended finite element method for the analysis of crack propagation in power modules. *Power Electron. Devices Compon.* **2023**, *4*, 100027. [\[CrossRef\]](#)
- Wang, T.; Zhang, F.; Furtney, J.; Damjanac, B. A review of methods, applications and limitations for incorporating fluid flow in the discrete element method. *J. Rock. Mech. Geotech. Eng.* **2022**, *14*, 1005–1024. [\[CrossRef\]](#)
- Radjai, F.; Dubois, F. *Discrete-Element Modeling of Granular Materials*; Wiley-Iste: Hoboken, NJ, USA, 2011.
- Wang, L.; Huang, S.; Gu, Q.; Sun, B.; Li, S.; Lin, Z. Simulation of highly nonlinear materials based on a stabilized non-ordinary state-based peridynamic model. *Soil Dyn. Earthq. Eng.* **2022**, *157*, 107250. [\[CrossRef\]](#)
- Sun, B.; Li, S.; Gu, Q.; Ou, J. Coupling of peridynamic and numerical substructure method for modeling structures with local discontinuities. *Comput. Model. Eng. Sci.* **2019**, *120*, 739–757. [\[CrossRef\]](#)
- Silling, S.A. Reformulation of elasticity theory for discontinuities and long-range forces. *J. Mech. Phys. Solids* **2000**, *48*, 175–209. [\[CrossRef\]](#)
- Huang, X.; Bie, Z.; Wang, L.; Jin, Y.; Liu, X.; Su, G.; He, X. Finite element method of bond-based peridynamics and its ABAQUS implementation. *Eng. Fract. Mech.* **2019**, *206*, 408–426. [\[CrossRef\]](#)
- Silling, S.A.; Askari, E. A meshfree method based on the peridynamic model of solid mechanics. *Comput. Struct.* **2005**, *83*, 1526–1535. [\[CrossRef\]](#)
- Huang, D.; Zhang, Q.; Qiao, P. Damage and progressive failure of concrete structures using non-local peridynamic modeling. *Sci. China Technol. Sci.* **2011**, *54*, 591–596. [\[CrossRef\]](#)
- Demmie, P.N.; Preece, D.S.; Silling, S.A. *Warhead Fragmentation Modeling with Peridynamics*; Sandia National Lab. (SNL-NM): Albuquerque, NM, USA, 2007.
- Zhang, N.; Gu, Q.; Huang, S.; Xue, X.; Li, S. A practical bond-based peridynamic modeling of reinforced concrete structures. *Eng. Struct.* **2021**, *244*, 112748. [\[CrossRef\]](#)
- Zheng, G.; Shen, G.; Xia, Y.; Hu, P. A bond-based peridynamic model considering effects of particle rotation and shear influence coefficient. *Int. J. Numer. Methods Eng.* **2020**, *121*, 93–109. [\[CrossRef\]](#)
- Bobaru, F.; Duangpanya, M. The peridynamic formulation for transient heat conduction. *Int. J. Heat. Mass. Transf.* **2010**, *53*, 4047–4059. [\[CrossRef\]](#)
- Mikata, Y. Peridynamics for fluid mechanics and acoustics. *Acta Mech.* **2021**, *232*, 3011–3022. [\[CrossRef\]](#)

16. Diyaroglu, C.; Oterkus, S.; Oterkus, E.; Madenci, E.; Han, S.; Hwang, Y. Peridynamic wetness approach for moisture concentration analysis in electronic packages. *Microelectron. Reliab.* **2017**, *70*, 103–111. [\[CrossRef\]](#)
17. Ni, T.; Zaccariotto, M.; Zhu, Q.-Z.; Galvanetto, U. Coupling of FEM and ordinary state-based peridynamics for brittle failure analysis in 3D. *Mech. Adv. Mater. Struct.* **2021**, *28*, 875–890. [\[CrossRef\]](#)
18. Sun, W.; Fish, J.; Zhang, G. Superposition of non-ordinary state-based peridynamics and finite element method for material failure simulations. *Meccanica* **2020**, *55*, 681–699. [\[CrossRef\]](#)
19. Gu, Q.; Wang, L.; Huang, S. Integration of peridynamic theory and openses for solving problems in civil engineering. *Comput. Model. Eng. Sci.* **2019**, *120*, 471–489. [\[CrossRef\]](#)
20. Lu, J.; Zhang, Y.; Muhammad, H.; Chen, Z.; Xiao, Y.; Ye, B. 3D analysis of anchor bolt pullout in concrete materials using the non-ordinary state-based peridynamics. *Eng. Fract. Mech.* **2019**, *207*, 68–85. [\[CrossRef\]](#)
21. Dong, Y.; Su, C.; Qiao, P. An improved mesoscale damage model for quasi-brittle fracture analysis of concrete with ordinary state-based peridynamics. *Theor. Appl. Fract. Mech.* **2021**, *112*, 102829. [\[CrossRef\]](#)
22. Gu, Q.; Lin, Z.; Wang, L.; Sun, B.; Pan, J. A practical stress correction method for improving stability of state-based peridynamics based on stress equilibrium equation. *Int. J. Struct. Stab. Dyn.* **2022**, *22*, 2250094. [\[CrossRef\]](#)
23. Li, P.; Hao, Z.; Zhen, W. A stabilized non-ordinary state-based peridynamic model. *Comput. Methods Appl. Mech. Eng. Technol.* **2018**, *339*, 262–280. [\[CrossRef\]](#)
24. Chowdhury, S.R.; Roy, P.; Roy, D.; Reddy, J. A modified peridynamics correspondence principle: Removal of zero-energy deformation and other implications. *Comput. Methods Appl. Mech. Eng.* **2019**, *346*, 530–549. [\[CrossRef\]](#)
25. Chen, H.; Spencer, B.W. Peridynamic bond-associated correspondence model: Stability and convergence properties. *Int. J. Numer. Methods Eng.* **2019**, *117*, 713–727. [\[CrossRef\]](#)
26. Silling, S.A. Stability of peridynamic correspondence material models and their particle discretizations. *Comput. Methods Appl. Mech. Eng.* **2017**, *322*, 42–57. [\[CrossRef\]](#)
27. Breitenfeld, M.S.; Geubelle, P.H.; Weckner, O.; Silling, S.A. Non-ordinary state-based peridynamic analysis of stationary crack problems. *Comput. Methods Appl. Mech. Eng.* **2014**, *272*, 233–250. [\[CrossRef\]](#)
28. Gu, Q.; Lin, Z.; Wang, L.; Huang, S.; Li, S. A stabilized hybrid peridynamic method compatible with constitutive models of different dimensions. *Soil. Dyn. Earthq. Eng.* **2023**, *172*, 107903. [\[CrossRef\]](#)
29. Xue, X.; Seki, H. Influence of longitudinal bar corrosion on shear behavior of RC beams. *J. Adv. Concr. Technol.* **2010**, *8*, 145–156. [\[CrossRef\]](#)
30. Silling, S.A.; Epton, M.; Weckner, O.; Xu, J.; Askari, E. Peridynamic states and constitutive modeling. *J. Elast.* **2007**, *88*, 151–184. [\[CrossRef\]](#)
31. Xin, X.; Seki, H.; Hiromori, S. Influence of reinforcing bar corrosion on shear behavior of rc beams. *Doboku Gakkai Ronbunshuu E* **2005**, *65*, 161–177.
32. Drucker, D.C.; Prager, W. Soil mechanics and plastic analysis or limit design. *Q. Appl. Math.* **1952**, *10*, 157–165. [\[CrossRef\]](#)
33. Schreppers, G.J.; Frissen, C.; Kang, H.J.; Prediction of Crack-Width and Crack-Pattern. TNO DIANA BV, The Netherlands. 2011. Available online: <https://dianafea.com/prediction-of-crack-width-crack-pattern/> (accessed on 20 June 2023).

Disclaimer/Publisher's Note: The statements, opinions and data contained in all publications are solely those of the individual author(s) and contributor(s) and not of MDPI and/or the editor(s). MDPI and/or the editor(s) disclaim responsibility for any injury to people or property resulting from any ideas, methods, instructions or products referred to in the content.